Optics & Laser Technology 180 (2025) 111427

Contents lists available at ScienceDirect

Optics and Laser Technology

journal homepage: www.elsevier.com/locate/optlastec

Research Note

Dissimilar laser welding of an as-rolled CoCrFeMnNi high entropy alloy to Inconel 718 superalloy

D. Afonso [a], J.G. Lopes [b,c,*], Y.T. Choi [d], R.E. Kim [d], N. Schell [e], N. Zhou [c], H.S. Kim [d,f], J. P. Oliveira [a,b,*]

[a] CENIMAT/I3N, Department of Materials Science, Faculty of Sciences and Technology, Universidade NOVA de Lisboa, Caparica 2829-516, Portugal
[b] UNIDEMI, Department of Mechanical and Industrial Engineering, NOVA School of Science and Technology, Universidade NOVA de Lisboa, Caparica 2829-516, Portugal
[c] Centre of Advanced Materials Joining, Department of Mechanical & Mechatronics Engineering, University of Waterloo, 200 University Avenue West, Waterloo, Ontario N2L 3G1, Canada
[d] Graduate Institute of Ferrous Technology, POSTECH (Pohang University of Science and Technology), Pohang 790-794, South Korea
[e] Institute of Materials Physics, Helmholtz-Zentrum Hereon, Max-Planck-Str. 1, Geesthacht D-21502, Germany
[f] Advanced Institute for Materials Research (WPI-AIMR), Tohoku University, Sendai 980-8577, Japan

ARTICLE INFO

Keywords:
CoCrFeMnNi
Inconel 718
High entropy alloys
Laser welding
Synchrotron X-ray diffraction

ABSTRACT

In this work, dissimilar laser welding between an as-rolled CoCrFeMnNi high entropy alloy (HEA) and Inconel 718 Ni-base superalloy was successfully performed. Defect-free joints with a tensile strength of 822 MPa and a fracture strain of 7.1 % were obtained. The microstructural analysis was conducted using scanning electron microscopy (SEM), electron backscattered diffraction (EBSD), energy-dispersive X-ray spectroscopy (EDS) and high energy synchrotron X-ray diffraction (SXRD), complemented by thermodynamic calculations using the CalPhaD methodology. Mechanical assessment of the joints was conducted via microhardness mapping and tensile testing, allowing to unveil processing-microstructure-properties relationships. Although the precipitation of the Laves phase was identified within the fusion zone, our results reveal the excellent dissimilar weldability between the two alloys, allowing the deployment of this dissimilar material pair for structural applications.

High entropy alloys (HEAs) are novel class of materials known for its revolutionary way to enable new alloy compositions significantly different from those commonly used in conventional engineering alloys [1]. Among the several HEAs that have already been discovered, the equiatomic CoCrFeMnNi HEA, also known as the Cantor alloy, stands as the first HEA to have been reported [2,3]. Throughout the years, the CoCrFeMnNi alloy has shown remarkable properties depending on its processing conditions. The interesting properties associated to these materials include high strength at extreme temperatures [4], notable wear resistance [5] and excellent corrosion resistance [6].

The advancements on CoCrFeMnNi-based HEAs research further potentialize its integration in key engineering applications. Furthermore, such premise can be accomplished by studying the weldability of HEAs, since the possibility of using them to create complex structures is very appealing to industry and welding is a widely used technique for such endeavor [7–9]. On this topic, literature shows that an effort to understand (and control) the metallurgical changes occurring in the CoCrFeMnNi HEA during welding have already been conducted in both similar [10–14] and dissimilar combinations [15–22]. As such, in this work, we study the weldability of a dissimilar laser welded joint between an as-rolled CoCrFeMnNi alloy and Inconel 718 Ni-based superalloy by detailing its microstructure and unraveling its mechanical behavior.

The choice of Inconel 718 to be coupled to the CoCrFeMnNi HEA is based on its high strength and corrosion resistant characteristics which makes it a competitive choice for several industrial sectors such as aerospace, gas turbines, and oil & gas [23–26]. In this regard, our results address the lack of comprehension regarding the compatibility of the CoCrFeMnNi alloy with Inconel 718 which, to the best of the authors knowledge, has not been addressed to this point in the literature.

* Corresponding authors at: UNIDEMI, Department of Mechanical and Industrial Engineering, NOVA School of Science and Technology, Universidade NOVA de Lisboa, Caparica 2829-516, Portugal. CENIMAT/I3N, Department of Materials Science, Faculty of Sciences and Technology, Universidade NOVA de Lisboa, Caparica 2829-516, Portugal.
E-mail addresses: jcg.lopes@campus.fct.unl.pt (J.G. Lopes), jp.oliveira@fct.unl.pt (J.P. Oliveira).

https://doi.org/10.1016/j.optlastec.2024.111427
Received 16 April 2024; Received in revised form 4 June 2024; Accepted 5 July 2024

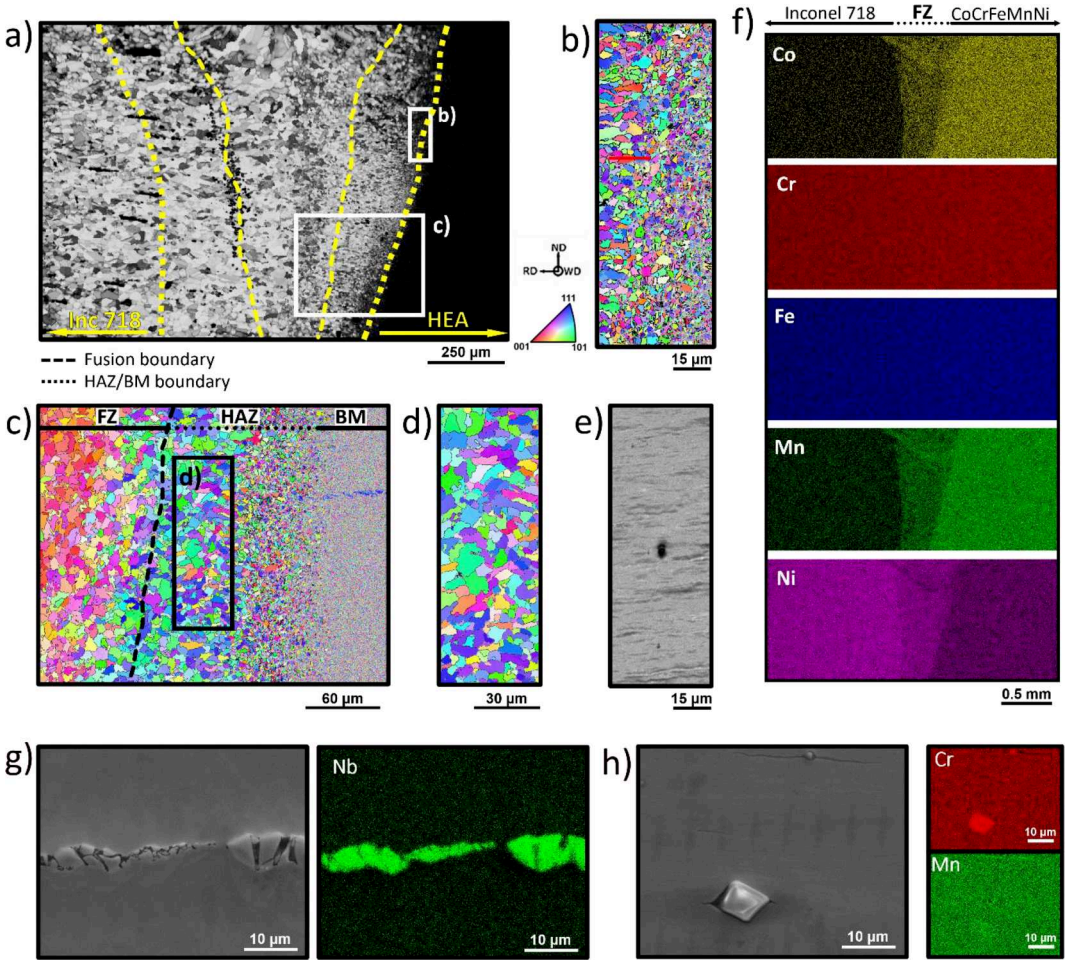

Fig. 1. Microstructure of the welded joint: a) SEM macrograph of the welded joint and corresponding EBSD IPF maps of the transition from the HAZ to the BM (b) and transition from the FZ to the HAZ (c) and detailed view of the HAZ (d); e) SEM micrograph of the BM; f) EDS maps the along the full extension of the welded joint. Additional detailed view and corresponding EDS maps of: g) NbC precipitates on the Inconel 718 BM and h) Cr-Mn oxides on the Cantor HEA BM.

For such, as-annealed Inconel 718 plates with a thickness of 1.5 mm were acquired from McMaster-Carr, while an as-rolled equiatomic CrMnFeCoNi high entropy alloy was fabricated from commercially pure elements and subjected to a thickness reduction of ≈50 % via cold-rolling (to a final thickness of 1.5 mm). Both materials were then cut via wire electron discharge machining to obtain 30 × 30 mm coupons which were used for laser welding.

Given this, the laser welding procedure was performed using a Miyachi Unitek LW50A pulsed Nd:YAG laser system, with a wavelength of 1.064 µm. A spot diameter of 600 µm and a peak power of 1.0 kW were used to obtain full penetration. Corresponding to a power density of ≈3.54 kW/mm^2 (calculated through the ratio between the peak power and the area of the beam [27,28]). The pulse profile had a duration of 10 ms, including 2 ms of up- and downslopes. Argon gas was applied at a flow rate of 0.57 m^3/h, to create a protective atmosphere surrounding the joint. A butt joint configuration was used.

For microstructural analysis, the joint cross section was analyzed using a JEOL JSM-7800F PRIME high-resolution field emission SEM equipped with backscattered electrons (BSE) and energy-dispersive X-ray spectroscopy (EDS) detectors. Electron backscatter diffraction (EBSD) analysis was performed using a FEI XL- 30S FEG SEM. Phase field mapping predictions using EDS data retrieved from the fusion zone (FZ) were calculated using the Scheil-Gulliver model available in Thermo-Calc [29] software, with the TCHEA5 database. Additionally, the full extension of the weld was scanned from one base material (BM) to the other using high energy synchrotron X-ray diffraction (SXRD), performed at the P07 beamline at PETRAIII/DESY. The beam spot size was set to 150 × 150 µm, with a 150 µm distance between consecutively analyzed spots. The X-ray beam had an energy of 87.1 keV (corresponding to a wavelength of 0.14235 Å) and the sample-to-detector distance was 1.365 m. The raw data was integrated using PyFAI [30] and analyzed using in-house developed python-based scripts.

To inspect the (local) mechanical properties, microhardness mapping was performed using a Mitutoyo Micro Hardness Testing Machine HM-112, with an indentation load of 300 g held for 10 s. The space between consecutive indentations was set to 125 µm in the longitudinal and transverse directions. Tensile testing was conducted on an Autograph Shimadzu AG50kNG machine, equipped with a 50 kN load cell at a 0.01 mm/s cross-head speed. Three repeats were performed to assess the joints reliability. The fracture surfaces were then analyzed using a Hitachi SU8000 SEM.

Fig. 1 depicts SEM imaging coupled with EBSD maps acquired from a representative cross section of the welded joint between Inconel 718 and the CoCrFeMnNi base materials (BMs). As observed, full penetration with no defects such as cracks or pores was obtained, potentially indicating a good weldability between the two alloys.

Comparing both BMs, the Inconel 718 BM has an average grain size of ≈15.1 ± 1.4 µm, while in the case of the CoCrFeMnNi HEA, the highly deformed condition of the grains hiders the acquisition of the Kikuchi patterns, inhibiting the quantification of grain size on this side (see Fig. 1e)). However, previous work on the same BM revealed that the CoCrFeMnNi HEA possessed pancake-shaped grains with an average

Table 1
Average chemical composition of Inconel 718 and CoCrFeMnNi BMs and the FZ, obtained via EDS, considering the elements detailed in Fig. 1.

Composition (at%)	Co	Cr	Fe	Mn	Ni	Nb
Inconel 718	≈0	22.5	19.8	≈0	54.5	2.8
CoCrFeMnNi	20.1	21.6	19.3	19.0	20.0	—
FZ	13.4	22.0	19.5	11.3	32.7	1.0

grain size approaching ≈2 μm [19].

Going closer from each of the BMs to the FZ, the heat affected zones (HAZ) arise. The HAZ is often associated with solid state transformation phenomena, such as grain growth and recrystallization, due to the relatively high temperatures (below complete melting) experienced by the material [31]. However, laser welding is known for its high cooling rates and reduced heat source dimensions resulting in a narrow HAZ extensions, which when associated to the different thermal conductivities of each BMs, may result in disparities in both grain size and shape of the HAZ on each side of the FZ. Such is the case in the present dissimilar welded joint. On the Inconel 718 side, the HAZ possesses an average grain size of ≈16.4 ± 0.8 μm and an extension of ≈265 ± 22 μm. On the CoCrFeMnNi side, as it is possible to observe in Fig. 1c), the transition from the BM to the FZ is made evident, where a relatively shorter HAZ can be observed (≈195 ± 33μm μm), with the grain size reaching values up to ≈4.5 ± 0.9 μm. Additionally, the differences in HAZ extension can also be related to the varying thermal conductivity values of both BMs with temperature. In fact, at temperatures under ≈900 °C, the thermal conductivity of the CoCrFeMnNi HEA tends to be slightly lower than that of the Inconel 718 BM, as calculated based on the compositions available in Table 1 and ThermoCalc software (refer to the Supplementary Material for the variation of thermal conductivity for both BM with temperature).

Attention is now directed to the FZ, where both BM experienced full melting and mixing during welding. Given the dissimilar nature of the BMs, this region presents itself as the most prone to generate intermetallic compounds that can hinder the overall performance of the joint. In the present case the shape of the FZ highlights a keyhole welding mode, where the length of the FZ is larger than its width. A keyhole FZ is caused by the high energy laser density applied on the interface of both materials to achieve full penetration [15]. Focusing on the inverse pole figure (IPF) map in Fig. 1c), the color displayed by the FZ present itself with a red tone indicating grain orientation in the ⟨001⟩, which indeed corresponds to the easy growth direction of FCC materials [32,33].

Furthermore, EDS maps taken across the welded joint are displayed in Fig. 1f). Comparably, the Cr and Fe maps showcase that the amount of each of these elements is similar in both BMs and in the FZ. The same does not occur for the other elements, where evidently Co and Mn are present in higher amount in the HEA side, while Ni is more evident on the Inconel 718 BM. Such agrees with what is known from the elemental contents of both BMs. Qualitatively, the FZ showcases the presence of all the aforementioned elements, although exhibiting a lower amount of Co and Mn than the HEA BM, and a lower amount of Ni than the Inconel 718 BM. This occurs due to a dilution effect induced by melting and mixing of the two BMs. It is, nonetheless, obvious that the Ni content in the FZ is higher than in the HEA BM. The average composition of both BMs and the FZ is detailed in Table 1.

Fig. 2a) displays the results obtained by consecutively probing the full extension of the welds using SXRD. This enabled to highlight the differences occurring in the diffraction patterns (obtained via full azimuthal integration) due to the varying microstructure across the joint.

Regarding phase identification, it is possible to see that both BMs are composed of a FCC matrix phase. Furthermore, consistent with Fig. 1g) and h), the presence of Mn-Cr oxides on the CoCrFeMnNi HEA and NbC precipitates in the Inconel 718 BM is also noticeable throughout the diffraction patterns. It is however, in the FZ, that the existence of a Laves (C14) intermetallic phase is visible (refer to Fig. 2b)), indicating that the FZ is not composed of a simple FCC solid solution, as it would be expected from HEAs given their often inherent solid solution effect [34].

To further investigate the phases present within the joint, CalPhaD-based thermodynamic calculations were performed using the non-equilibrium Scheil-Gulliver methodology, as shown in Fig. 2d) and e). For such, a consecutive series of EDS point measurements were gathered along the red dashed lines marked in Fig. 2d). These compositional data points where then used to obtain the temperature interval between the moment when the Liquid phase starts to solidify and when it reaches a total phase fraction of 0.01 %, and number of phases present at the final stages of solidification. By analyzing this data, it is possible to perceive that regarding the BMs, the Cantor HEA side is only expected to exhibit a single FCC phase, while the Inconel 718 superalloy showcases a total of three phases within its microstructure, these being the matrix FCC

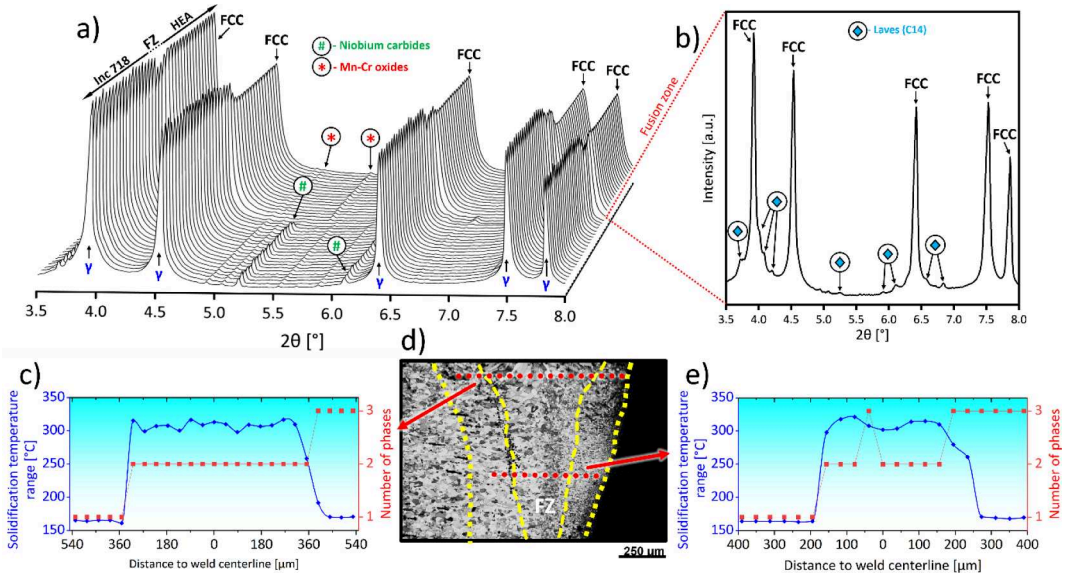

Fig. 2. Phase identification and distribution across the welded joint: a) Superimposition of the SXRD patterns along the whole extension of the weld; b) representative SXRD pattern of the FZ; c) CalPhaD-predicted phase distribution at the top of the joint, which is located in d), alongside with the e) phase distribution prediction at the middle of the joint.

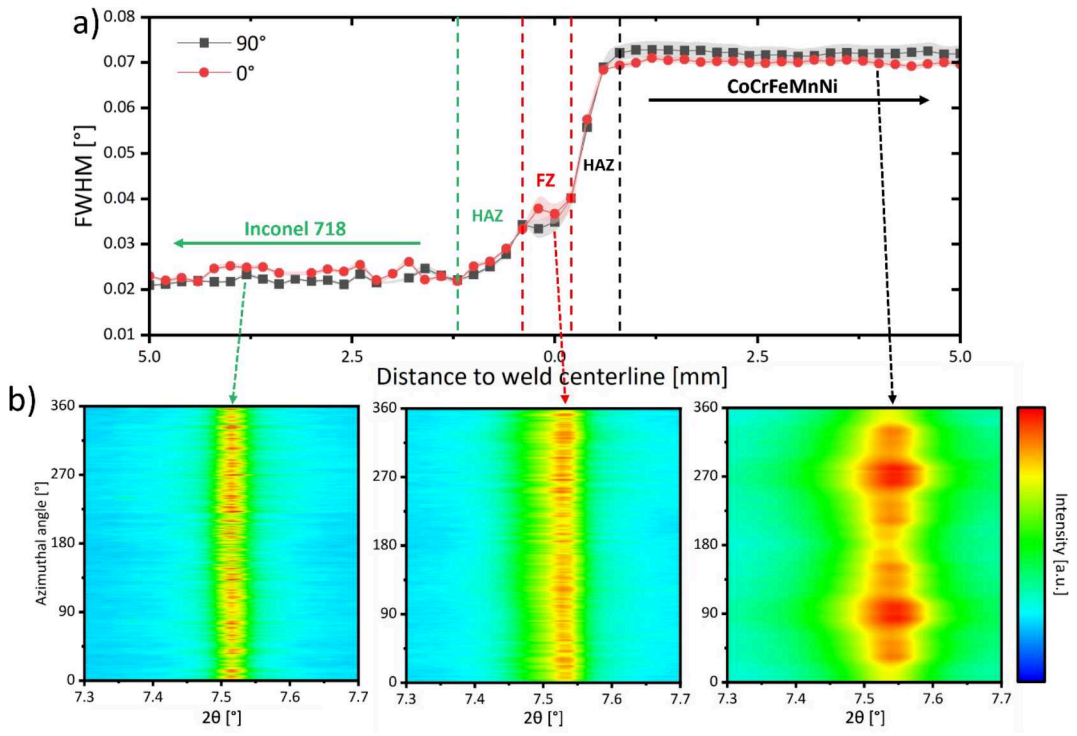

Fig. 3. a) FWHM variation of the (3 1 1) diffraction peak measured on the 0° and 90° azimuthal angles along the welded joint. b) Comparison between the diffraction data obtained on the FZ and both BM, obtained by integrating in 1° segments along the azimuthal angle.

phase, a Laves (C14) phase and an orthorhombic $D0_a$ phase (also known as δ phase [35]) rich in both Nb and Ni. This $D0_a$ structure, however, was not identified via SXRD, which can be explained by the fact that the of Nb content comes from the precipitates that are visible in Fig. 1g) and Fig. 2a).

It is in the FZ that these calculations are more relevant, as it is this region that undergoes fast and non-equilibrium solidification conditions due to the laser welding process, compounded by the complex mixing of the original BMs. As such, in the two measured lines it is possible to perceive that the mixture between the compositions of both alloys results in a higher solidification temperature range (approximately 300 °C) than the two dissimilar bulk BMs. Such differences in composition can be qualitatively viewed in Fig. 1f), and allow to perceive a higher risk for solidification cracking to occur in FZ, although no such defects were observed in the present joints.

Furthermore, considering the number of phases generated in the FZ upon the final stages of solidification, it can be observed that only two phases are formed, these being an FCC phase and a Laves (C14). These results are compliant with the phase identification using SXRD shown in Fig. 2a). Interestingly, in Fig. 2d), one single point indicates the formation of three phases, where the third phase corresponds to the $D0_a$ (δ) phase structure. This indicates that the local composition in this region is closer to the Inconel 718 BM, possibly due to elemental segregation or molten pool dynamics associated with the Marangoni effect [36]. Nevertheless, going further into the evenly dispersed Laves (C14) phase on both the FZ and Inconel 718 BM, the literature indicates that the Nb content (which has a higher atomic radius) is critical in its formation in Inconel 718 [37,38]. Such allows us to assume that the same factor can be expected in the FZ.

Additionally, observing the maximum peak intensity values in Fig. 2a) (corresponding, in this case, to the peak height) of the FZ, the influence of the different grain size and morphology between both BMs is demonstrated. In fact, while the more refined CoCrFeMnNi BM exhibits a constant intensity distribution with increasing distance from the FZ, the Inconel 718 side exhibits a higher variability on the maximum intensity values. Nevertheless, a deeper insight on the effect of grain size and structural defects on the SXRD data will be provided further ahead in Fig. 3 when considering the full width at half maximum (FWHM) variation of the (3 1 1) diffraction peak.

As such, the evolution of the FWHM of the (3 1 1) peak was obtained by integrating from 10° segments along the 0° and 90° azimuthal angles, corresponding to the welding direction and the direction perpendicular to it (refer to [10] for more details on the SXRD experimental procedure). These results are shown in Fig. 3. This was performed since the FWHM relates the broadening effect on the diffraction peaks caused by the combined influence of the internal strains, imposed by structural defects (such as dislocations and stacking faults) and the size of the sub-grain structures, which diffract light coherently within a grain and are often referred to as crystallites [31]. Due to the possibility of imperfect alignment between these sub-grain structures due to residual stresses, radiation is reflected on a divergent but nearby 2θ angle, causing the diffraction peaks to broaden, thus affecting peak width. A higher value of FWHM, thus translates to a superior level of structural defects and/or to smaller sized sub-structures within the grains. Given this, analysis of this parameter along the joint can help understand the microstructural variations caused by the process heat input. In this case, although each peak will have its own preferred orientation after solidification of the molten pool, which is reign by epitaxial and competitive grain growth, we only display the distribution of the (3 1 1) peak FWHM due to its insensitivity to intergranular strains [32].

As it is possible to observe the FWHM variation on the Inconel 718 BM is ≈2.8 times lower than the FWHM displayed in the CoCrFeMnNi BM. Such agrees with the microstructural condition of both BMs highlighted in Fig. 1a), where the Inconel 718 is in the annealed condition and the CoCrFeMnNi HEA is in the as-rolled condition. Between the two BMs, the gradual increase in FWHM from the Inconel 718 to the CoCrFeMnNi side evidences the structural modifications in terms of grains morphology, size and structural defects that occurs in both the HAZs and the FZ. Furthermore, it can, once again, be evidenced that the extension of the HAZ is larger in the Inconel 718 side, reaching 0.8 mm indicating that the effects of the high temperatures on the HAZ are larger than those observed by SEM.

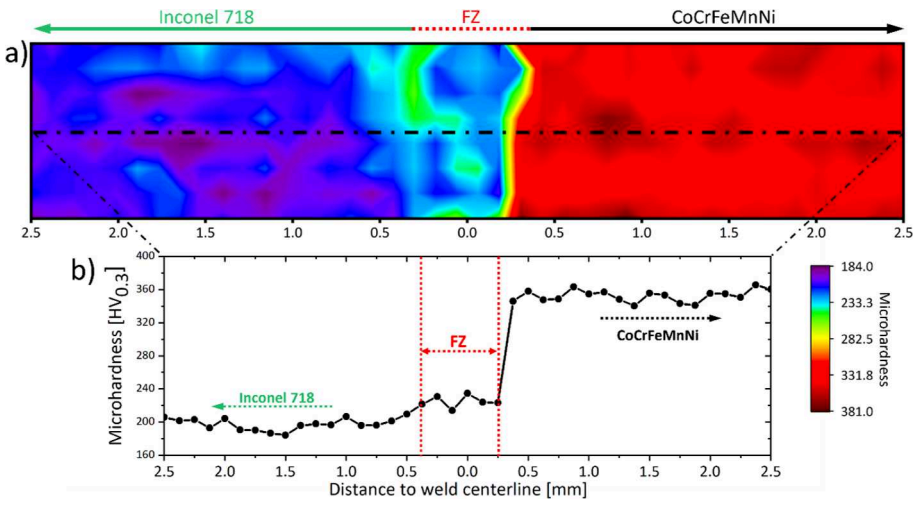

Fig. 4. a) Microhardness distribution along the welded joint and b) corresponding microhardness distribution measured at mid height.

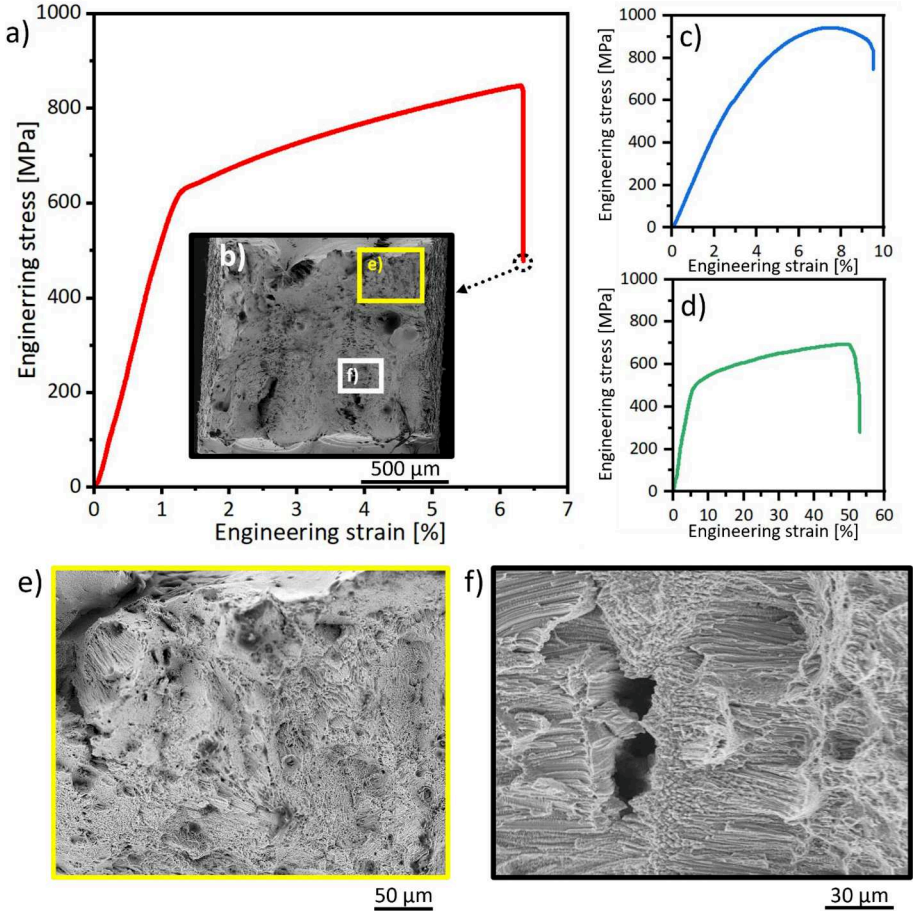

Fig. 5. a) Representative stress–strain curve of the welded joint tensile and macroscopic view of the fracture surface (b); c) and d) are representative stress–strain curves for the rolled CoCrFeMnNi and annealed Inconel 718 BMs, respectively. e) and f) corresponding to detailed views of the macroscopic fracture surface shown in b).

On a different note, the 2θ angle peak distribution of the (3 1 1) peak in regard to the azimuthal angle can be observed in Fig. 3b), which was obtained by integrating the raw diffraction data into 1° segments. For the Inconel 718 case, the consistent distribution of the peaks along the full azimuthal range indicates a relatively stress-free condition of this BM. The same, however, cannot be said regarding the CoCrFeMnNi BM, as it clearly shown that the diffraction peak distribution showcases a preferential orientation towards the 90° and 270° angles, which are aligned with the rolling process direction to which the HEA was submitted prior to welding, thus evidencing a strong texture effect caused by it.

Finally, the FZ evidences a similar diffraction peak distribution to the Inconel 718 BM throughout the azimuthal range, indicating that upon solidification the (3 1 1) grains of the FZ do not evidence any preferential

Table 2
Summary of the welded joint mechanical properties of both BM and dissimilar welded joint.

Material	Yield strength [MPa]	Ultimate tensile strength [MPa]	Fracture strain [%]
CoCrFeMnNi HEA (from [19])	587 ± 7	943 ± 6	9.5 ± 0.2
Inconel 718	461.4 ± 16	743 ± 52	48.4 ± 7.7
Welded joints	614 ± 35	822 ± 63	7.1 ± 0.4

orientation, probably due to the fast-cooling rate of laser welding which restricts the formation of large and highly aligned grains, as opposed to arc-based processes.

With the microstructural condition of the welded joint highlighted, the next step is to evaluate how the local mechanical response of the weld is affected by the microstructure changes imposed by the weld thermal cycle. For such, Fig. 4 displays the variation in microhardness along the joint. While Inconel 718 (in the as-annealed condition) reaches values surrounding 208 ± 12 $HV_{0.3}$, the microhardness of the CoCrFeMnNi BM goes up to 343 ± 9 $HV_{0.3}$, as a result of the impact on of the high dislocation density induced by the cold rolling process. Interestingly, despite the fact that the grain size of the FZ should produce the lowest microhardness values on the joint, the solid solution effect granted by the mixture between the two BMs causes intermediate microhardness values between the two BMs (and above that of as-cast CoCrFeMnNi HEA) to occur in this region, yielding a microhardness of approximately 220 ± 35 $HV_{0.3}$.

A representative stress/strain curve for the dissimilar joint is shown in Fig. 5a) alongside with the tensile curves of the BMs (see Fig. 5c) and d)). The yield strength (YS), ultimate tensile strength (UTS) and fracture strain values for both BMs and dissimilar joint are summarized in Table 2.

Comparing both BMs, it is possible to observe that the CrMnFeCoNi HEA achieves higher stress levels than the Inconel 718, while exhibiting significantly lower fracture strain values. Additionally, considering the tensile properties of the welded joints, it can be observed that its UTS reaches intermediate values between the two BMs, however showcasing the lowest elongation to fracture amongst all cases. This can be explained by the fact that the chemical composition of its FZ is a combination of the two BMs (see Fig. 1f)), thus allowing the joints to sustain similar levels of stress, which is in line with the hardness distribution in the welded joints. On the other hand, such can also explain the lower elongation to fracture exhibited by the joints, which can be further hindered by the presence of Laves (C14) particles in the FZ.

Regarding the fracture surface, Ni-based superalloys and CrMnFeCoNi HEAs commonly fail by ductile fracture processes [10,11,24,25]. However, from Fig. 5b), e), and f) the fracture surfaces present themselves as a mixture of ductile and brittle-like fracture presented by the dimples and rivers patterns in the analyzed regions. Such is granted by the relatively smaller grains and the presence of intermetallic phases of the FZ. Given this, although the main fracture mechanism is ductile, the presence of the Laves (C14) phase may contribute to the embrittlement of the joint. Such indicates the relatively lower plastic deformation tolerance of the welded joint, although exhibiting excellent mechanical properties for a dissimilar joint.

Overall, dissimilar laser welding between an as-rolled CoCrFeMnNi HEA and Inconel 718 was successfully accomplished. Analysis of the microstructure allowed to unveil the microstructural differences between both BMs and the features arising on the HAZ and FZ due to the high temperatures developed during laser welding. Interestingly, the nucleation of a Laves (C14) phase was observed by means of SXRD and confirmed by CalPhaD simulations. Regarding the mechanical behavior, the FZ exhibited an intermediate microhardness level between both BMs, due to the combined effect of varying grain morphology and the compositional mixture between the BMs. Tensile testing indicated that the welded samples could endure stresses up to ≈822 ± 63 MPa eventually fracturing at strain of ≈7.1 ± 0.4 %, showcasing their potential use as part of structural components.

Declaration of competing interest

The authors declare that they have no known competing financial interests or personal relationships that could have appeared to influence the work reported in this paper.

Data availability

The raw/processed data required to reproduce these findings cannot be shared at this time as the data also forms part of an ongoing study. Data will be made available on request.

Acknowledgement

JGL and JPO acknowledges Fundação para a Ciência e a Tecnologia (FCT - MCTES) for its financial support via the project UID/00667/2020 (UNIDEMI). JL acknowledges Fundação para a Ciência e a Tecnologia (FCT - MCTES) for funding the Ph.D. grant 2020.07350. BD. JPO and DA acknowledges the funding by national funds from FCT - Fundação para a Ciência e a Tecnologia, I.P., in the scope of the projects LA/P/0037/2020, UIDP/50025/2020 and UIDB/50025/2020 of the Associate Laboratory Institute of Nanostructures, Nanomodelling and Nanofabrication – i3N. This work was supported by the National Research Foundation of Korea (NRF) grant funded by the Korea government (MSIP) (NRF-2021R1A2C3006662). The authors acknowledge DESY (Hamburg, Germany), a member of the Helmholtz Association HGF, for the provision of experimental facilities. Beamtime was allocated for proposal I-20221211 EC. The research leading to this result has been supported by the project CALIPSOplus under the Grant Agreement 730872 from the EU Framework Programme for Research and Innovation HORIZON 2020.

Appendix A. Supplementary data

Supplementary data to this article can be found online at https://doi.org/10.1016/j.optlastec.2024.111427.

References

[1] I. Baker, B. Cantor, J.-W. Yeh, High entropy alloys and materials, High Entropy Alloys & Materials 2023 (1) (2023) 1–3, https://doi.org/10.1007/S44210-023-00019-7.
[2] J.W. Yeh, S.K. Chen, S.J. Lin, J.Y. Gan, T.S. Chin, T.T. Shun, C.H. Tsau, S.Y. Chang, Nanostructured high-entropy alloys with multiple principal elements: novel alloy design concepts and outcomes, Adv. Eng. Mater. 6 (2004) 299–303, https://doi.org/10.1002/ADEM.200300567.
[3] B. Cantor, I.T.H. Chang, P. Knight, A.J.B. Vincent, Microstructural development in equiatomic multicomponent alloys, Mater. Sci. Eng. A 375–377 (2004) 213–218, https://doi.org/10.1016/J.MSEA.2003.10.257.
[4] Z. Han, W. Ren, J. Yang, Y. Du, R. Wei, C. Zhang, Y. Chen, G. Zhang, The deformation behavior and strain rate sensitivity of ultra-fine grained CoNiFeCrMn high-entropy alloys at temperatures ranging from 77 K to 573 K, J. Alloy. Compd. 791 (2019) 962–970, https://doi.org/10.1016/J.JALLCOM.2019.03.373.
[5] J. Joseph, N. Haghdadi, M. Annasamy, S. Kada, P.D. Hodgson, M.R. Barnett, D. M. Fabijanic, On the enhanced wear resistance of CoCrFeMnNi high entropy alloy at intermediate temperature, Scr. Mater. 186 (2020) 230–235, https://doi.org/10.1016/J.SCRIPTAMAT.2020.05.053.
[6] H. Thota, R. Jeyaraam, L.R. Bairi, A.S. Tirunilai, A. Kauffmann, J. Freudenberger, M. Heilmaier, S. Mandal, S.S. Vadlamani, Grain boundary engineering and its implications on corrosion behavior of equiatomic CoCrFeMnNi high entropy alloy, J. Alloy. Compd. 888 (2021) 161500, https://doi.org/10.1016/J.JALLCOM.2021.161500.
[7] J.G. Lopes, J.P. Oliveira, A short review on welding and joining of high entropy alloys, Metals (Basel) 10 (2020) 212, https://doi.org/10.3390/met10020212.
[8] A. Hamada, S. Ghosh, M. Ali, M. Jaskari, A. Järvenpää, Studying the strengthening mechanisms and mechanical properties of dissimilar laser-welded butt joints of medium-Mn stainless steel and automotive high-strength carbon steel, Mater. Sci. Eng. A 856 (2022) 143936, https://doi.org/10.1016/J.MSEA.2022.143936.

[9] J.P. Oliveira, T.G. Santos, R.M. Miranda, Revisiting fundamental welding concepts to improve additive manufacturing: From theory to practice, Prog. Mater Sci. 107 (2020) 100590, https://doi.org/10.1016/J.PMATSCI.2019.100590.
[10] J.P. Oliveira, T.M. Curado, Z. Zeng, J.G. Lopes, E. Rossinyol, J.M. Park, N. Schell, F. M. Braz Fernandes, H.S. Kim, Gas tungsten arc welding of as-rolled CrMnFeCoNi high entropy alloy, Mater. Des. 189 (2020), https://doi.org/10.1016/j.matdes.2020.108505.
[11] Z. Wu, S.A. David, D.N. Leonard, Z. Feng, H. Bei, Microstructures and mechanical properties of a welded CoCrFeMnNi high-entropy alloy, Sci. Technol. Weld. Join. 23 (2018) 585–595, https://doi.org/10.1080/13621718.2018.1430114.
[12] J.Y. Lin, Z.H. Lai, T. Otsuki, H.W. Yen, S. Nambu, Gradient microstructure and interfacial strength of CoCrFeMnNi high-entropy alloy in solid-state ultrasonic welding, Mater. Sci. Eng. A 825 (2021) 141885, https://doi.org/10.1016/J.MSEA.2021.141885.
[13] R. Li, P. Niu, T. Yuan, P. Cao, C. Chen, K. Zhou, Selective laser melting of an equiatomic CoCrFeMnNi high-entropy alloy: Processability, non-equilibrium microstructure and mechanical property, J. Alloy. Compd. 746 (2018) 125–134, https://doi.org/10.1016/J.JALLCOM.2018.02.298.
[14] S. Park, H. Nam, J. Park, Y. Na, H. Kim, N. Kang, Superior-tensile property of CoCrFeMnNi alloys achieved using friction-stir welding for cryogenic applications, Mater. Sci. Eng. A 788 (2020) 139547, https://doi.org/10.1016/J.MSEA.2020.139547.
[15] J.P. Oliveira, A. Shamsolhodaei, J. Shen, J.G. Lopes, R.M. Gonçalves, M. de Brito Ferraz, L. Piçarra, Z. Zeng, N. Schell, N. Zhou, H. Seop Kim, Improving the ductility in laser welded joints of CoCrFeMnNi high entropy alloy to 316 stainless steel, Mater. Des. 219 (2022) 110717. Doi: 10.1016/J.MATDES.2022.110717.
[16] H. Do, S. Asadi, N. Park, Microstructural and mechanical properties of dissimilar friction stir welded CoCrFeMnNi high entropy alloy to STS304 stainless steel, Mater. Sci. Eng. A 840 (2022) 142979, https://doi.org/10.1016/J.MSEA.2022.142979.
[17] J. Shen, R. Gonçalves, Y.T. Choi, J.G. Lopes, J. Yang, N. Schell, H.S. Kim, J. P. Oliveira, Microstructure and mechanical properties of gas metal arc welded CoCrFeMnNi joints using a 410 stainless steel filler metal, Mater. Sci. Eng. A 857 (2022) 144025, https://doi.org/10.1016/J.MSEA.2022.144025.
[18] J. Shen, R. Gonçalves, Y.T. Choi, J.G. Lopes, J. Yang, N. Schell, H.S. Kim, J. P. Oliveira, Microstructure and mechanical properties of gas metal arc welded CoCrFeMnNi joints using a 308 stainless steel filler metal, Scr. Mater. 222 (2023) 115053, https://doi.org/10.1016/J.SCRIPTAMAT.2022.115053.
[19] J.P. Oliveira, J. Shen, Z. Zeng, J.M. Park, Y.T. Choi, N. Schell, E. Maawad, N. Zhou, H.S. Kim, Dissimilar laser welding of a CoCrFeMnNi high entropy alloy to 316 stainless steel, Scr. Mater. 206 (2022) 114219, https://doi.org/10.1016/J.SCRIPTAMAT.2021.114219.
[20] N.K. Adomako, G. Shin, N. Park, K. Park, J.H. Kim, Laser dissimilar welding of CoCrFeMnNi-high entropy alloy and duplex stainless steel, J. Mater. Sci. Technol. 85 (2021) 95–105, https://doi.org/10.1016/J.JMST.2021.02.003.
[21] H. Nam, S. Park, N. Park, Y. Na, H. Kim, S.J. Yoo, Y.H. Moon, N. Kang, Weldability of cast CoCrFeMnNi high-entropy alloys using various filler metals for cryogenic applications, J. Alloy. Compd. 819 (2020) 153278, https://doi.org/10.1016/J.JALLCOM.2019.153278.
[22] H. Nam, S. Park, E.-J. Chun, H. Kim, Y. Na, N. Kang, Laser dissimilar weldability of cast and rolled CoCrFeMnNi high-entropy alloys for cryogenic applications, Sci. Technol. Weld. Join. (2019) 1–8, https://doi.org/10.1080/13621718.2019.1644471.
[23] T. Sonar, V. Balasubramanian, S. Malarvizhi, T. Venkateswaran, D. Sivakumar, An overview on welding of Inconel 718 alloy - Effect of welding processes on microstructural evolution and mechanical properties of joints, Mater. Charact. 174 (2021) 110997, https://doi.org/10.1016/J.MATCHAR.2021.110997.
[24] B. Kagay, K. Findley, S. Coryell, A.B. Nissan, Effects of alloy 718 microstructure on hydrogen embrittlement susceptibility for oil and gas environments, Mater. Sci. Technol. 32 (2016) 697–707, https://doi.org/10.1080/02670836.2016.1139225.
[25] K. Sajun Prasad, S.K. Panda, S.K. Kar, M. Sen, S.V.S.N. Murty, S.C. Sharma, Microstructures, forming limit and failure analyses of Inconel 718 sheets for fabrication of aerospace components, J. Mater. Eng. Perform. 26 (2017) 1513–1530, https://doi.org/10.1007/S11665-017-2547-4.
[26] M.A. Kattimani, P.R. Venkatesh, H. Masum, M.M. Math, V.N. Bahadurdesai, S. Mustafkhadri, C.D. Prasad, H. Vasudev, Design and numerical analysis of tensile deformation and fracture properties of induction hardened inconel 718 superalloy for gas turbine applications, Int. J. Interact. Des. Manuf. (2023) 1–11, https://doi.org/10.1007/S12008-023-01452-Z.
[27] E. Assuncao, S. Williams, D. Yapp, Interaction time and beam diameter effects on the conduction mode limit, Opt. Lasers Eng. 50 (2012) 823–828, https://doi.org/10.1016/J.OPTLASENG.2012.02.001.
[28] W.A. Ayoola, W.J. Suder, S.W. Williams, Parameters controlling weld bead profile in conduction laser welding, J. Mater. Process. Technol. 249 (2017) 522–530, https://doi.org/10.1016/J.JMATPROTEC.2017.06.026.
[29] J.O. Andersson, T. Helander, L. Höglund, P. Shi, B. Sundman, Thermo-Calc & DICTRA, computational tools for materials science, Calphad 26 (2002) 273–312, https://doi.org/10.1016/S0364-5916(02)00037-8.
[30] J. Kieffer, V. Valls, N. Blanc, C. Hennig, New tools for calibrating diffraction setups, Urn:1600-5775 27 (2020) 558–566, https://doi.org/10.1107/S1600577520000776.
[31] J.G. Lopes, P. Agrawal, J. Shen, N. Schell, R.S. Mishra, J.P. Oliveira, Evolution of microstructure and mechanical properties in gas tungsten arc welded dual-phase Fe50Mn30Co10Cr10 high entropy alloy, Mater. Sci. Eng. A 878 (2023) 145233, https://doi.org/10.1016/J.MSEA.2023.145233.
[32] J.G. Lopes, P. Rocha, D.A. Santana, J. Shen, E. Maawad, N. Schell, F.G. Coury, J. P. Oliveira, Impact of arc-based welding on the microstructure evolution and mechanical properties in newly developed Cr29.7Co29.7Ni35.4Al4Ti1.2 multi-principal element alloy, Adv. Eng. Mater. (2023) 2300109, https://doi.org/10.1002/ADEM.202300109.
[33] S. Kou, Weld. Metall. (2002), https://doi.org/10.1002/0471434027.
[34] D.B. Miracle, O.N. Senkov, A critical review of high entropy alloys and related concepts, Acta Mater. 122 (2017) 448–511, https://doi.org/10.1016/j.actamat.2016.08.081.
[35] S. Mahadevan, S. Nalawade, J.B. Singh, A. Verma, B. Paul, K. Ramaswamy, Evolution of δ phase microstructure in alloy 718, in: 7th International Symposium on Superalloy 718 and Derivatives, 2010, pp. 737–750, https://doi.org/10.1002/9781118495223.CH57.
[36] J.P. Oliveira, Z. Zeng, C. Andrei, F.M. Braz Fernandes, R.M. Miranda, A.J. Ramirez, T. Omori, N. Zhou, Dissimilar laser welding of superelastic NiTi and CuAlMn shape memory alloys, Mater. Des. 128 (2017) 166–175, https://doi.org/10.1016/J.MATDES.2017.05.011.
[37] S. Sui, H. Tan, J. Chen, C. Zhong, Z. Li, W. Fan, A. Gasser, W. Huang, The influence of Laves phases on the room temperature tensile properties of Inconel 718 fabricated by powder feeding laser additive manufacturing, Acta Mater. 164 (2019) 413–427, https://doi.org/10.1016/J.ACTAMAT.2018.10.032.
[38] Y. Zhang, Z. Li, P. Nie, Y. Wu, Effect of cooling rate on the microstructure of laser-remelted INCONEL 718 coating, Metall. Mater. Trans. A 44 (2013) 5513–5521, https://doi.org/10.1007/S11661-013-1903-8.